


Unconventional specular optical rotation in the charge ordered state of Kagome metal CsV_3Sb_5

Received: 25 April 2023

Accepted: 23 August 2023

Published online: 01 September 2023

 Check for updatesCamron Farhang¹, Jingyuan Wang¹ , Brenden R. Ortiz², Stephen D. Wilson² & Jing Xia¹ 

Kagome metals AV_3Sb_5 ($A = \text{K}, \text{Cs}, \text{Rb}$) provide a rich platform for intertwined orders, where evidence for time-reversal symmetry breaking, likely due to the long-sought loop currents, has emerged in STM and muon spin relaxation experiments. An isotropic component in the spontaneous optical rotation has also been reported and was interpreted as the magneto-optic Kerr effect. Intriguingly, the observed rotations differ by five orders of magnitude between different wavelengths and samples, suggesting more intricate physics. Here we report optical rotation and polar Kerr measurements in CsV_3Sb_5 crystals at the same wavelength. We observe large isotropic components of 1 milliradian in the optical rotation that do not respond to applied magnetic fields, while the spontaneous Kerr signal is less than 20 nanoradians. Our results prove unambiguously that the reported isotropic rotation is not from time-reversal symmetry breaking but represents the long-sought specular optical rotation and indicates a new intertwined order.

The Kagome lattice is a rich platform for novel phases of matter due to the interplay between strong correlation and topological orders, such as in the case of Chern topological magnet TbMn_6Sn_6 ¹. In particular the recently discovered quasi-two-dimensional Kagome compounds AV_3Sb_5 ($A = \text{K}, \text{Rb}$ and Cs)^{2,3} have elaborate phase diagrams due to the ideal Kagome network governed by layers of vanadium and antimony intercalated by alkali metal ions^{2,3}. The fascinating electronic band structure containing Dirac cones, flat bands, and Van Hove singularities^{3,4} leads to intertwined⁵ electronic instabilities and exhibits charge density wave (CDW)^{6–10}, pressure-tunable superconductivity^{3,11–14}, and time reversal symmetry breaking (TRSB) that has been revealed by STM¹⁵ and muon spin relaxation (μSR)^{16–18} experiments. The TRSB state may be related to the long-sought loop currents^{19,20}, and could produce a spontaneous magneto-optic Kerr effect (MOKE)^{21,22} rotation θ_K , which arises from the optical phase difference $\Delta\varphi = 2\theta_K$ between counter-propagating circularly polarized light beams that are time-reversal images of each other.

Indeed, two optical rotation experiments performed at 800 nm wavelength have revealed^{23,24} a spontaneous total rotation θ_T in the form of $\theta_T = \theta_C + \theta_p \sin(2\alpha - A)$, where α is the incident polarization

angle, and A is the principle axis direction. θ_p represents the anisotropic component due to the nematicity^{23,24} of the CDW state. Since translational symmetry is also broken, it will be called “anisotropy” in this work to avoid confusion. θ_C represents the isotropic (polarization independent) component and was found to be 0.5 mrad²⁴ and 50 μrad ²³ in CsV_3Sb_5 . In transmission, such an isotropic θ_C component could arise from optical activities in a chiral material, which causes an optical phase difference between circularly polarized lights propagating in the same direction. However, this effect is usually rejected²⁵ in normal incidence reflection used in the above experiments. Therefore, the observed isotropic rotation θ_C has been naturally attributed to a spontaneous MOKE signal θ_K due to TRSB at T_{CDW} ^{23,24}. Intriguingly, it is noted²⁴ that such a large θ_C can be compared with that of some magnetic materials, while both μSR ^{16–18} experiments and theoretical calculations²⁶ indicate extremely small sub-gauss level magnetic flux density that would usually lead to nano-radians to sub-microradian levels of spontaneous MOKE signals^{27,28}. Dedicated MOKE experiments^{29–31} have been carried out in CsV_3Sb_5 at 1550 nm wavelength utilizing zero-loop Sagnac interferometers³² in an attempt to

¹Department of Physics and Astronomy, University of California, Irvine, CA 92697, USA. ²Materials Department, University of California, Santa Barbara, Santa Barbara, CA 93106, USA. ✉ e-mail: xia.jing@uci.edu

resolve this puzzle. Such an interferometer is sensitive only to TRSB effects by detecting the optical phase difference $\Delta\varphi$ between time-reversed counter-propagating circularly polarized light beams, which is twice the MOKE angle: $\Delta\varphi = 2\theta_K$. Surprisingly the 1550 nm MOKE experiments report either a much smaller spontaneous Kerr signal $\theta_K \sim 2 \mu\text{rad}^{30}$ or near-zero values $\theta_K < 0.03 \mu\text{rad}^{29,31}$. To explain this giant discrepancy, one is tempted to assume a resonance enhancement at 800 nm wavelength over 1550 nm. On the contrary the near-infrared spectra of CsV_3Sb_5 are rather flat^{33,34} with a Lorentz resonance at 6000 cm^{-1} (equivalent to 1667 nm)³⁴ suggesting instead a larger expected signal at the 1550 nm wavelength.

To solve this outstanding mystery, we perform optical rotation and polar MOKE measurements at 1550 nm wavelength on the same CsV_3Sb_5 crystals. Rather surprisingly, we observe giant $\theta_C \sim \pm 1200 \mu\text{rad}$ below T_{CDW} but negligible $\theta_K < 0.02 \mu\text{rad}$ at zero magnetic fields. The θ_C component does not respond to applied magnetic fields, which is opposite to MOKE and to the magnetic field responses found in STM¹⁵ and μSR^{16-18} experiments. Therefore, we conclude that the observed θ_C represents an unconventional optical rotation that is not due to either TRSB, anisotropy or chiral order, but originates from a new intertwined order that onsets at T_{CDW} .

Results

CDW transition

High quality CsV_3Sb_5 single crystals, dubbed sample 1 and 2, were grown by the self-flux method at UCSB³. The first order CDW transition at $T_{CDW} \sim 94 \text{ K}$ is clearly characterized by sharp peaks in the heat capacity C_p and resistance derivative dR/dT as shown in Fig. 1e. The crystals were cleaved perpendicular to the *c*-axis to expose optically flat areas and were mounted to the sample stage using Ge-varnish for minimal strain.

Optical rotation and MOKE

As shown in Fig. 1a, a standard optical setup based on a Wollaston prism is used to measure the optical rotation (θ_T) as a function of incident polarization angle α . And a zero-loop Sagnac interferometer³² as shown in Fig. 2a is used for polar MOKE (θ_K) detection and imaging. Both instruments are connected to the same optical cryostat so θ_T and θ_K can be obtained from the same region in the sample during one experiment. Operation and calibration of both instruments on several test samples are described in the Supplementary Information. As shown in Fig. S2, the resolution of θ_T and θ_K are $30 \mu\text{rad}$ and $0.02 \mu\text{rad}$, respectively. And they agree within 2% on the MOKE signal of a magnetic film test sample. The root cause for the Sagnac interferometer's superior sensitivity is that it only measures microscopic TRSB and rejects any non-TRSB effects such as anisotropy. This is because the sourcing aperture for one light is the receiving aperture for the other time-reversed counterpropagating light, both apertures being the same single mode optical fiber. Hence Onsager's relations guarantee zero signal in the absence of microscopic TRSB. Such rejection of non-TRSB effect is demonstrated in Fig. S2e to the $0.04 \mu\text{rad}$ level with an anisotropic polymer film, which displays anisotropic polarization rotations with twofold rotational symmetry of $\pm 20 \text{ mrad}$.

We first examine CsV_3Sb_5 sample 1, whose optical rotation and MOKE results are summarized in Figs. 1, 2, respectively. At $B = 0$, polar plots of $\theta_T(\alpha)$ at representative temperatures are shown in Fig. 1b, with additional temperatures plotted in Fig. S3a-l. Below T_{CDW} , the total rotation θ_T contains an anisotropic component θ_p and an isotropic component θ_C , similar to the findings at the 800 nm wavelength^{23,24}. Fitted values of θ_p and θ_C are plotted in Fig. 1d showing sharp onsets just below T_{CDW} . The θ_p component originates from the reduction from sixfold rotational symmetry to 2-fold in the CDW state. Since electronic nematicity was found^{35,36} in CsV_3Sb_5 at much lower temperatures, θ_p is likely of structural origin. The size of θ_p is 0.2 mrad in our 1550 nm measurement. It should scale linearly with the anisotropies in the

permittivity and magneto-electric tensors³⁷ and inversely with the wavelength λ . The rather flat near-infrared spectra^{33,34} of CsV_3Sb_5 suggest that the former factor is comparable between 800 nm and 1550 nm. Hence, θ_p is expected to roughly double at 800 nm reaching 0.4 mrad , which indeed falls between the experimentally reported values of 0.9 mrad^{24} and 0.2 mrad^{23} at 800 nm.

What comes as a surprise is the size of the isotropic component θ_C , which has been interpreted as MOKE (θ_K) in the 800 nm experiments^{23,24} and is expected to be vanishingly small at 1550 nm. Instead, the observed θ_C as plotted in Fig. 1(d) reaches 1.4 mrad , which is larger than the reported values^{23,24} at 800 nm. A MOKE signal, which arises from TRSB, should flip sign with opposite magnetic fields. In contrast, we found no such response in θ_C : as shown in Fig. 1(c) with $\pm 0.3 \text{ T}$ applied magnetic fields, the change of optical rotation $\Delta\theta_T$ is much smaller than θ_C , approaching the noise level. This field-insensitivity is also opposite to the TRSB signatures reported in both STM¹⁵ and μSR^{16-18} experiments, which show clear magnetic responses. All these observations are suggestive that the isotropic component θ_C reported in^{23,24} and in this work is not MOKE and is not related to TRSB.

The decisive evidence that θ_C is not MOKE comes from Sagnac measurements of the same sample. As explained earlier, a Sagnac interferometer is only sensitive to MOKE, which is a direct result of TRSB. Figure 2c, d is θ_K images of the same region in sample 1 at 3 K with $B = 0.3 \text{ T}$ and $B = 0$, respectively. In the optically flat region where the reflected optical power (Fig. 2(b)) $P_0 > 1 \mu\text{W}$, the MOKE signal is uniform with $\theta_K \sim 7 \mu\text{rad}$ in $B = 0.3 \text{ T}$, and vanishes after the field is removed. θ_K is found to be paramagnetic and the MOKE susceptibility θ_K/B remains field-independent during cooldowns as shown in Fig. 2e. In another study³¹ we verified this paramagnetic MOKE response at fields up to 9 T . The absence of a Curie-Weiss shape in θ_K/B leads us to attribute it to the Pauli paramagnetism. And the sharp drop in θ_K/B from $32 \mu\text{rad}/\text{T}$ to $27 \mu\text{rad}/\text{T}$ at T_{CDW} is likely due to a decreased density of states in the CDW phase, which agrees with the reported reduction of magnetic susceptibility³. The magnetic fields were removed at the base temperature, and the subsequent zero field warmups (ZFW) are plotted in Fig. 2f. We observe no onset of spontaneous θ_K at T_{CDW} with an uncertainty of $0.02 \mu\text{rad}$, which is five orders of magnitude smaller than the observed $\theta_C \sim 1.4 \text{ mrad}$ in the same sample.

The sign of θ_C is also unrelated to that of θ_K , and appears to have already been determined during crystal growth. On the same crystal, we have always found the same sign of θ_C , regardless of direction of applied magnetic fields. The sign of θ_C can flip between samples. One such example can be found in CsV_3Sb_5 sample 2. The polarization rotations $\theta_T(\alpha)$ of sample 2 are mostly negative, as shown for representative temperatures in Fig. 3a, and for additional temperatures in Fig. S4a-o. The fitted anisotropic component θ_p and isotropic component θ_C are plotted in Fig. 3b, both showing sharp onsets at T_{CDW} . The low-temperature value of θ_p (0.2 mrad) is comparable to that in sample 1, while $\theta_C \sim -1.2 \text{ mrad}$ is similar in size but opposite in sign to that found in sample 1. The size of θ_C is also comparable to the 0.5 mrad value reported in a 800 nm experiment²⁴ where θ_C of the same sign and similar sizes were found in two CsV_3Sb_5 samples. Interestingly in another 800 nm experiment²³, θ_C of different signs and sizes up to 0.05 mrad were observed at different locations in a CsV_3Sb_5 sample. This can be explained if multi-domains of "sample 1" type and "sample 2" type are present in their sample, which will lead to location-dependent values of $\pm\theta_C$, and even intermediate values for sub-wavelength ($1 \mu\text{m}$) domains. It may also explain why their measured θ_C ²³ is one order of magnitude smaller than possible "single domain" samples in this work and in ref. 24. The sign of θ_C remains unchanged after thermal cycles in both samples 1 and 2, which agrees with the findings in the above 800 nm experiment²³ that thermal cycles at the same location do not change θ_C . In contrast, the MOKE signals θ_K (Fig. 3f) flip sign with opposite fields and are identical to those

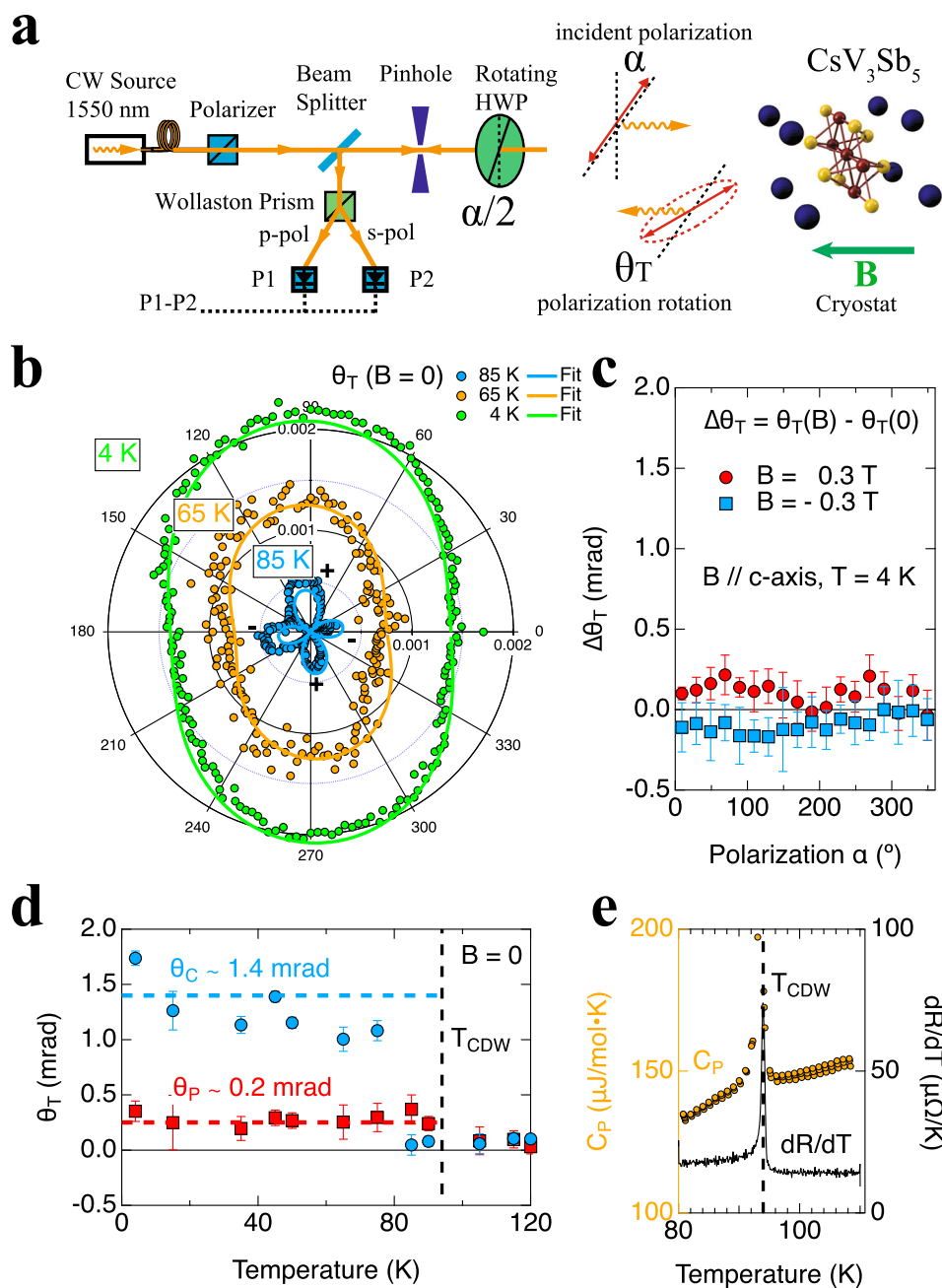


Fig. 1 | Optical rotation θ_T of CsV₃Sb₅ sample 1. a Polarization rotation θ_T at normal incidence is measured as a function of incident polarization angle α . See SI for details. **b** Polar plots of spontaneous θ_T at representative temperatures, fitted with $\theta_T = \theta_C + \theta_P \sin(2\alpha - A)$. See Fig. S3a–I for full data. **c** Changes of rotation $\Delta\theta_T$ by ± 0.3 T magnetic fields at 4 K, showing opposite magnetic fields fail to flip the sign of

θ_C , where error bars represent standard deviation. **d** Fitted θ_C (θ_P) up to 1.4 mrad (0.2 mrad) with onsets below T_{CDW} , where error bars represent uncertainty in fitting. **e** $T_{CDW} \sim 94$ K is marked by sharp peaks in the specific heat C_P and resistance derivative dR/dT .

measured in sample 1. At zero magnetic field the change of spontaneous θ_K across T_{CDW} is below 0.02 μ rad (Fig. 3g), which also agrees with the findings in sample 1.

Discussion

With these observations, we conclude that the isotropic polarization component $\theta_C \sim \pm(1.3 \pm 0.1)$ mrad is not MOKE, which is five orders of magnitude smaller. And the sign of θ_C , unlike the MOKE signal θ_K , is unrelated to the direction of applied magnetic fields, but seems to have been predetermined at crystal growth. Therefore, θ_C is not related to the proposed TRSB loop currents^{19,20} or experimentally observed TRSB signatures in both STM¹⁵ and μ SR^{16–18} experiments. Being isotropic, θ_C also does not originate from

anisotropy, which gives rise to the anisotropic component $\theta_P \sim 0.2$ mrad.

The expected MOKE signal estimated from the sub-Gauss level internal magnetic field measured in μ SR^{16–18} experiments is at the nanoradian to sub-microradian level^{27,28} if the loop currents^{19,20} order ferromagnetically between adjacent layers. Since antiferromagnetic interlayer ordering may be more favorable energetically, the expected MOKE signal from TRSB may be much smaller, falling below our sensitivity of 0.02 μ rad. The TRSB signature can still be detected by STM¹⁵ that probes the top layer, and μ SR^{16–18} that senses local fields. Optical resonance enhancements would likely be needed for Sagnac MOKE to detect a TRSB signal that would require the operation in the Terahertz, which hasn't been developed yet.

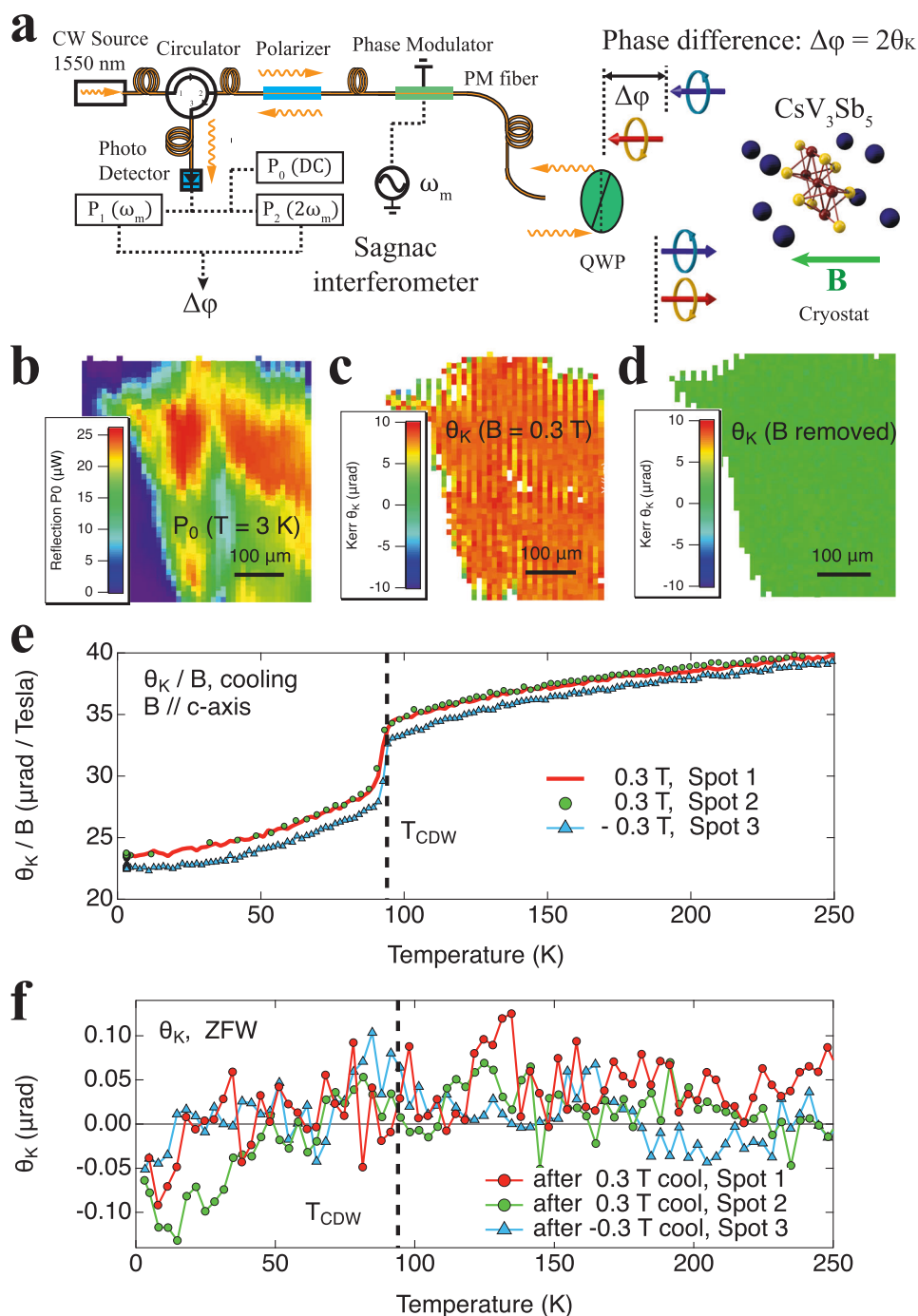


Fig. 2 | MOKE θ_K in CsV₃Sb₅ sample 1. **a** MOKE signal θ_K is measured by a Sagnac interferometer during the same experiment. See SI for details. **b, c** Scanning images of reflected optical power P_0 and MOKE θ_K at 3 K in $B = 0.3$ T showing uniform θ_K in the reflective regions. **d** Image of θ_K after removal of the magnetic field, showing

zero spontaneous MOKE signal across the sample. **e** θ_K/B during cooldown at a few locations and magnetic fields showing a paramagnetic MOKE response that drops sharply below T_{CDW} . **f** No onset of spontaneous θ_K at T_{CDW} was found during subsequent zero field warmup (ZFW).

The observed θ_C , an isotropic specular optical rotation at normal incidence without MOKE, represents new physics beyond TRSB or any other order discussed in AV₃Sb₅. The very existence of this unconventional optical effect, often referred to as specular (reflection) optical rotation³⁸, is a matter of long-standing debate and is usually rejected²⁵ in the context of ordinary optical materials. It was theoretically proposed to exist in strongly absorbing nematic materials and was reported in α -HgS (cinnabar) at 543 nm, close to the bandgap energy³⁸. However, neither the 1550 nm or the 800 nm wavelength is close to a band gap in CsV₃Sb₅^{33,34}. In addition, it has been shown³⁹ that a nematic material such as cinnabar would not

produce such isotropic rotation. Instead³⁹, for nematic materials with optical activity the rotation is proportional to the difference of the magneto-electric tensor³⁷ components $k_{xx} - k_{yy}$ perpendicular to the propagation direction z , which is the c -axis of CsV₃Sb₅. As such, the resulting optical rotation would flip sign when the incidence polarization angle α is rotated by 90°, which is incompatible with the isotropic nature of θ_C . In fact, this nematic optical activity could produce an optical rotation $\propto (k_{xx} - k_{yy}) \cos(2\alpha)$ (see discussions in the Supplementary Information) that would explain the puzzling sinusoidal form of the anisotropic rotation component $\theta_P \sin(2\alpha - A)$.

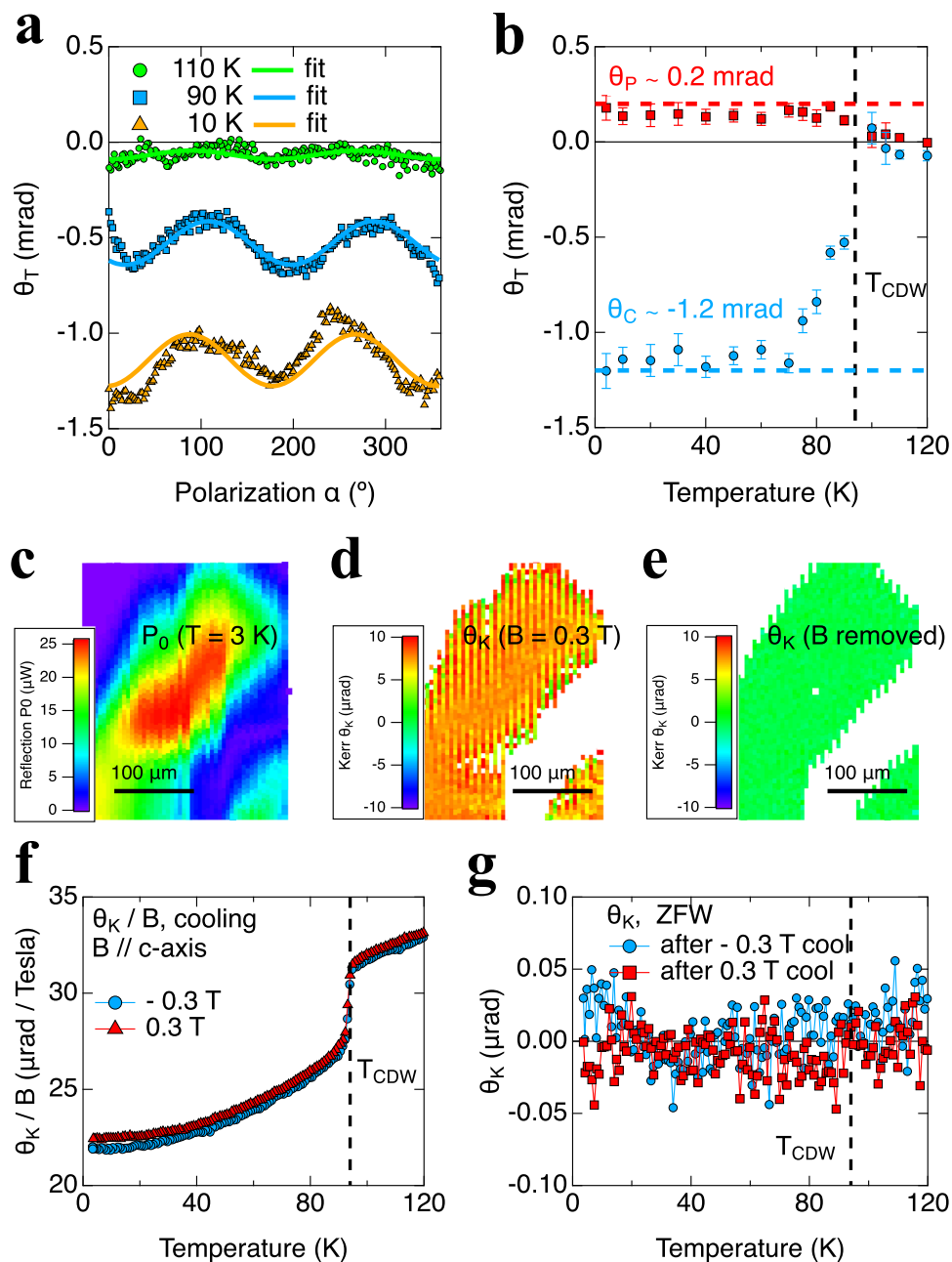


Fig. 3 | Optical rotation and MOKE in another CsV₃Sb₅ sample 2 with negative θ_C . **a** Spontaneous θ_T at representative temperatures, fitted with $\theta_T = \theta_C + \theta_P \sin(2\alpha - A)$. See Fig. S4a–o for full data. **b** Fitted θ_C (θ_P) up to -1.2 mrad (0.2 mrad) with onsets below T_{CDW} , where error bars represent uncertainty in fitting. Note the

negative sign of θ_C . **c–e** are scanning images of P_0 , θ_K with $B = 0.3$ T, and θ_K after field removal, all at 3 K. **f, g** are averaged traces of θ_K/B during field cooldowns and of spontaneous θ_K during subsequent ZFW. See SI for full data. There is no observable onset of spontaneous θ_K at T_{CDW} with an uncertainty of 0.02 μrad .

Hence the observed isotropic θ_C does not originate from a chiral order such as a cholesteric CDW state but is the first clear demonstration of the long-sought isotropic specular optical rotation not found in any other material system to our knowledge. And this isotropic rotation θ_C observed at 800 nm^{23,24} and at 1550 nm in this work either indicates a new intertwined order, or represents a novel hybrid phenomenon from the complex intertwining of the various orders in the CDW state. The topological Kagome lattice⁴⁰ is indeed full of surprises.

Methods

High-quality CsV₃Sb₅ single crystals were grown by the self-flux method at UCSB. Heat capacity and electrical transport measurements were performed with a Quantum Design Physical Property

Measurement System (PPMS) at UC Irvine. Both polarization rotation and MOKE measurements were performed in an optical cryostat without breaking vacuum at UC Irvine, where polarization rotation is measured with the standard Wollaston prism method, and MOKE is conducted with a fiber-optics Sagnac interferometer microscope. Both optical instruments' working principles are briefly described below, and their operation, performance, and cross-checking are detailed in the Supplementary Information. They operate with continuous wave (CW) light sources at the 1550 nm wavelength, with typical optical powers of 100 μW in the polarization rotation setup and 20 μW in the Sagnac interferometer.

The polarization rotation setup is shown in Fig. 1(a). The beam of light is routed through a free-space polarizer to produce a

linearly polarized beam. A polarization-independent beam splitter (half mirror) transmits half of the beam and reflects the other half, which is discarded. The transmitted beam passes through a pinhole and then a half-wave plate (HWP), which is mechanically rotated such that its principal fast axis is at an angle $\alpha/2$ to the polarization direction of the beam. The resulting beam after the HWP has its polarization direction rotated by angle α . The beam then passes through the optical window of the cryostat and gets reflected by the sample. The returned light beam passing the same pinhole a second time is in general elliptical with the major axis rotated by the total polarization rotation $\alpha + \theta_T$. After passing through the HWP a second time, its polarization direction is rotated by $-\alpha$, and becomes θ_T . And the same polarization-independent beam splitter reflects half the returned beam towards a Wollaston prism, which separates and directs two orthogonal polarizations s and p toward two balanced detectors. The recorded powers of s and p-polarization components are P1 and P2 respectively. The Wollaston prism is rotated at a $\pi/4$ angle such that with a gold mirror calibration sample P1 and P2 are “balanced”: $\Delta P = P1 - P2 = 0$. The optical amplitudes E1 and E2 at detectors 1 and 2 are:

$$E1 = E0 \cos\left(\frac{\pi}{4} - \theta_T\right) \quad (1)$$

$$E2 = E0 \cos\left(\frac{\pi}{4} + \theta_T\right) \quad (2)$$

where E0 is the total amplitude. Since optical intensity $I = E^2$, the sum and difference of the two intensities I1 and I2 are:

$$I1 + I2 = E1^2 + E2^2 = E0^2 \cos^2\left(\frac{\pi}{4} + \theta_T\right) + E0^2 \cos^2\left(\frac{\pi}{4} - \theta_T\right) = E0^2 \quad (3)$$

$$I1 - I2 = E1^2 - E2^2 = E0^2 \cos^2\left(\frac{\pi}{4} - \theta_T\right) - E0^2 \cos^2\left(\frac{\pi}{4} + \theta_T\right) = E0^2 \sin(2\theta_T) \quad (4)$$

Hence:

$$\frac{I1 - I2}{I1 + I2} = \sin(2\theta_T) \quad (5)$$

As optical power is proportional to intensity $P \propto I$, we can extract θ_T as:

$$\theta_T = \frac{1}{2} \arcsin\left(\frac{I1 - I2}{I1 + I2}\right) = \frac{1}{2} \arcsin\left(\frac{P1 - P2}{P1 + P2}\right) = \frac{1}{2} \arcsin\left(\frac{\Delta P}{P1 + P2}\right) \quad (6)$$

The MOKE measurement is performed using a zero-loop fiber-optic Sagnac interferometer as shown in Fig. 2a. The beam of light is routed by a fiber circulator to a fiber polarizer. After the polarizer the polarization of the beam is at 45° to the axis of a fiber-coupled electro-optic modulator (EOM), which generates 4.6 MHz time-varying phase shifts $\phi_m \sin(\omega t)$, where the amplitude $\phi_m = 0.92$ rad between the two orthogonal polarizations that are then launched into the fast and slow axes of a polarization maintaining (PM) single-mode fiber. Upon exiting the fiber, the two orthogonally polarized linearly polarized beams are converted into right- and left-circularly polarizations by a quarter-wave plate (QWP) and are then focused onto the sample. After reflection from the sample, the same QWP converts the reflected beams back into linear polarizations with exchanged polarization axes. The two beams then pass

through the PM fiber and EOM but with exchanged polarization modes in the fiber and the EOM. At this point, the two beams have gone through the same path but in opposite directions, except for a phase difference of $\Delta\phi$ from reflection off the magnetic sample and another time-varying phase difference by the modulation of EOM. This nonreciprocal phase shift $\Delta\phi$ between the two counter-propagating circularly polarized beams upon reflection from the sample is twice the Kerr rotation $\Delta\phi = 2\theta_K$. The two beams are once again combined at the detector and interfere to produce an optical signal $P(t)$:

$$P(t) = \frac{1}{2} P[1 + \cos(\Delta\phi + \phi_m \sin(\omega t))] \quad (7)$$

where P is the returned power if the modulation by the EOM is turned off. For MOKE signals that are slower than the 4.590 MHz modulation frequency used in this experiment, we can treat $\Delta\phi$ as a slowly time-varying quantity. And $P(t)$ can be further expanded into Fourier series with the first few orders listed below:

$$P(t)/P = \frac{1}{2} [1 + J_0(2\phi_m)] + (\sin(\Delta\phi)J_1(2\phi_m)) \sin(\omega t), + (\cos(\Delta\phi)J_2(2\phi_m)) \cos(2\omega t) + 2J_3(2\phi_m) \sin(3\omega t) + \dots \quad (8)$$

where $J_1(2\phi_m)$ and $J_2(2\phi_m)$ are Bessel J-functions. Lock-in detection was used to measure the first three Fourier components: the average (DC) power (P0), the first harmonics (P1), and the second harmonics (P2). And the Kerr rotation can then be extracted using the following formula:

$$\theta_K = \frac{1}{2} \Delta\phi = \frac{1}{2} \tan^{-1} \left[\frac{J_2(2\phi_m)P1}{J_1(2\phi_m)P2} \right] \quad (9)$$

Reporting summary

Further information on research design is available in the Nature Portfolio Reporting Summary linked to this article.

Data availability

Source data are provided with this paper. They have been deposited in a figshare repository with <https://doi.org/10.6084/m9.figshare.23575155>.

References

1. Yin, J.-X. et al. Quantum-limit Chern topological magnetism in TbMn6Sn6. *Nature* **583**, 533–536 (2020).
2. Ortiz, B. R. et al. New kagome prototype materials: discovery of KV3Sb5, RbV3Sb5, and CsV3Sb5. *Phys. Rev. Mater.* **3**, 094407 (2019).
3. Ortiz, B. R. et al. CsV3Sb5: A Z2 Topological Kagome Metal with a Superconducting Ground State. *Phys. Rev. Lett.* **125**, 247002 (2020).
4. Kang, M. et al. Twofold van Hove singularity and origin of charge order in topological kagome superconductor CsV3Sb5. *Nat. Phys.* **18**, 301–308 (2022).
5. Fradkin, E., Kivelson, S. A. & Tranquada, J. M. *Colloquium: Theory of intertwined orders in high temperature superconductors*. *Rev. Mod. Phys.* **87**, 457–482 (2015).
6. Stahl, Q. et al. Temperature-driven reorganization of electronic order in CsV3Sb5. *Phys. Rev. B* **105**, 195136 (2022).
7. Ortiz, B. R. et al. Fermi surface mapping and the nature of charge-density-wave order in the Kagome superconductor CsV3Sb5. *Phys. Rev. X* **11**, 041030 (2021).

8. Liang, Z. et al. Three-dimensional charge density wave and surface-dependent vortex-core states in a kagome superconductor CsV₃Sb₅. *Phys. Rev. X* **11**, 031026 (2021).
9. Li, H. et al. Observation of unconventional charge density wave without acoustic phonon anomaly in Kagome superconductors AV₃Sb₅ (A=Rb, Cs). *Phys. Rev. X* **11**, 031050 (2021).
10. Xiao, Q. et al. Coexistence of multiple stacking charge density waves in kagome superconductor CsV₃Sb₅. *Phys. Rev. Res.* **5**, L012032 (2023).
11. Yu, F. H. et al. Unusual competition of superconductivity and charge-density-wave state in a compressed topological kagome metal. *Nat. Commun.* **12**, 3645 (2021).
12. Zheng, L. et al. Emergent charge order in pressurized kagome superconductor CsV₃Sb₅. *Nature* **611**, 682–687 (2022).
13. Du, F. et al. Pressure-induced double superconducting domes and charge instability in the kagome metal KV₃Sb₅. *Phys. Rev. B* **103**, L220504 (2021).
14. Wang, N. N. et al. Competition between charge-density-wave and superconductivity in the kagome metal RbV₃Sb₅. *Phys. Rev. Res.* **3**, 043018 (2021).
15. Jiang, Y.-X. et al. Unconventional chiral charge order in kagome superconductor KV₃Sb₅. *Nat. Mater.* **20**, 1353–1357 (2021).
16. Khasanov, R. et al. Time-reversal symmetry broken by charge order in CsV₃Sb₅. *Phys. Rev. Res.* **4**, 023244 (2022).
17. Mielke, C. et al. Time-reversal symmetry-breaking charge order in a kagome superconductor. *Nature* **602**, 245–250 (2022).
18. Shan, Z. et al. Muon spin relaxation study of the layered kagome superconductor CsV₃Sb₅. *Phys. Rev. Res.* **4**, 033145 (2022).
19. Haldane, F. D. M. Model for a quantum hall effect without landau levels: Condensed-matter realization of the ‘Parity Anomaly’. *Phys. Rev. Lett.* **61**, 2015–2018 (1988).
20. Varma, C. M. Non-Fermi-liquid states and pairing instability of a general model of copper oxide metals. *Phys. Rev. B* **55**, 14554–14580 (1997).
21. Bader, S. D. Smoke. *J. Magn. Magn. Mater.* **100**, 440–454 (1991).
22. Qiu, Z. Surface magneto-optic Kerr effect (SMOKE). *J. Magn. Magn. Mater.* **200**, 664–678 (1999).
23. Xu, Y. et al. Three-state nematicity and magneto-optical Kerr effect in the charge density waves in kagome superconductors. *Nat. Phys.* 1470–1475 (2022).
24. Wu, Q. et al. Simultaneous formation of two-fold rotation symmetry with charge order in the kagome superconductor CsV₃Sb₅ by optical polarization rotation measurement. *Phys. Rev. B* **106**, 205109 (2022).
25. Bassiri, S., Papas, C. H. & Engheta, N. Electromagnetic wave propagation through a dielectric–chiral interface and through a chiral slab. *J. Opt. Soc. Am. A, JOSAA* **5**, 1450–1459 (1988).
26. Denner, M. M., Thomale, R. & Neupert, T. Analysis of charge order in the Kagome metal AV₃Sb₅ (A = K, Rb, Cs). *Phys. Rev. Lett.* **127**, 217601 (2021).
27. Xia, J., Maeno, Y., Beyersdorf, P. T., Fejer, M. M. & Kapitulnik, A. High resolution polar Kerr effect measurements of Sr₂RuO₄: Evidence for broken time-reversal symmetry in the superconducting state. *Phys. Rev. Lett.* **97**, 167002 (2006).
28. Schemm, E. R., Gannon, W. J., Wishne, C. M., Halperin, W. P. & Kapitulnik, A. Observation of broken time-reversal symmetry in the heavy-fermion superconductor UPt₃. *Science* **345**, 190–193 (2014).
29. Saykin, D. R. et al. High resolution polar kerr effect studies of CsV₃Sb₅ tests for time reversal symmetry breaking below the charge order transition. *Phys. Rev. Lett.* **131**, 016901 (2023).
30. Hu, Y. et al. Time-reversal symmetry breaking in charge density wave of CsV₃Sb₅ detected by polar Kerr effect. Preprint at <http://arxiv.org/abs/2208.08036> (2022).
31. Wang, J., Farhang, C., Ortiz, B. R., Wilson, S. D. & Xia, J. Resolving the discrepancy between MOKE measurements at 1550-nm wavelength on Kagome Metal CsV₃Sb₅. Preprint at <https://doi.org/10.48550/arxiv.2301.08853> (2023).
32. Xia, J., Beyersdorf, P. T., Fejer, M. M. & Kapitulnik, A. Modified Sagnac interferometer for high-sensitivity magneto-optic measurements at cryogenic temperatures. *Appl. Phys. Lett.* **89**, 062508 (2006).
33. Uykur, E. et al. Low-energy optical properties of the non-magnetic kagome metal CsV₃Sb₅. *Phys. Rev. B* **104**, 045130 (2021).
34. Zhou, X. et al. Origin of charge density wave in the kagome metal CsV₃Sb₅ as revealed by optical spectroscopy. *Phys. Rev. B* **104**, L041101 (2021).
35. Zhao, H. et al. Cascade of correlated electron states in the kagome superconductor CsV₃Sb₅. *Nature* **599**, 216–221 (2021).
36. Nie, L. et al. Charge-density-wave-driven electronic nematicity in a kagome superconductor. *Nature* **604**, 59–64 (2022).
37. Condon, E. U. Theories of optical rotatory power. *Rev. Mod. Phys.* **9**, 432–457 (1937).
38. Bungay, A. R., Svirko, Yu. P. & Zheludev, N. I. Experimental observation of specular optical activity. *Phys. Rev. Lett.* **70**, 3039–3042 (1993).
39. Arteaga, O. Spectroscopic sensing of reflection optical activity in achiral AgGaS₂. *Opt. Lett.* **40**, 4277 (2015).
40. Yin, J.-X., Lian, B. & Hasan, M. Z. Topological kagome magnets and superconductors. *Nature* **612**, 647–657 (2022).

Acknowledgements

We acknowledge useful discussions with A. Kapitulnik. This project was supported by the Gordon and Betty Moore Foundation through Emergent Phenomena in Quantum Systems (EPiQS) Initiative Grant GBMF10276 (J.X.). S.D.W. and B.R.O. acknowledge support via the UC Santa Barbara NSF Quantum Foundry funded via the Q-AMASE-i program under award DMR-1906325 (S.D.W.).

Author contributions

C.F. carried out the Sagnac MOKE measurements. J.W. performed the thermal measurements. S.D.W. and B.R.O. grew the crystals. J.X. carried out the optical rotation measurements and wrote the paper.

Competing interests

The authors declare no competing interests.

Additional information

Supplementary information The online version contains supplementary material available at <https://doi.org/10.1038/s41467-023-41080-5>.

Correspondence and requests for materials should be addressed to Jing Xia.

Peer review information : *Nature Communications* thanks Yanfeng Guo, Qiong Wu and the other, anonymous, reviewer(s) for their contribution to the peer review of this work. A peer review file is available.

Reprints and permissions information is available at <http://www.nature.com/reprints>

Publisher’s note Springer Nature remains neutral with regard to jurisdictional claims in published maps and institutional affiliations.

Open Access This article is licensed under a Creative Commons Attribution 4.0 International License, which permits use, sharing, adaptation, distribution and reproduction in any medium or format, as long as you give appropriate credit to the original author(s) and the source, provide a link to the Creative Commons license, and indicate if changes were made. The images or other third party material in this article are included in the article's Creative Commons license, unless indicated otherwise in a credit line to the material. If material is not included in the article's Creative Commons license and your intended use is not permitted by statutory regulation or exceeds the permitted use, you will need to obtain permission directly from the copyright holder. To view a copy of this license, visit <http://creativecommons.org/licenses/by/4.0/>.

© The Author(s) 2023